

The completed High-Low framework for interface state density analysis in MOS capacitors

B. D. Rummel^{1,a,*}, S. Dhar², R. J. Kaplar¹

¹ Sandia National Laboratories, Albuquerque, New Mexico 87123, USA

² Department of Physics, Auburn University, Auburn, Alabama 36849, USA

^{a)} Author to whom correspondence should be addressed: bdrumme@sandia.gov

Interface state densities, D_{IT} , in metal-oxide-semiconductor (MOS) capacitors are rarely reported in the accumulation energy range. It is recognized that the determination of D_{IT} in accumulation is fundamentally obscured by small inaccuracies in the user-defined oxide capacitance, C_{OX} . This source of error prevents the High-Low frequency technique from reporting accumulation D_{IT} , even for sufficiently fast high-frequency measurements. To resolve this, an electrostatic constraint that is uniquely satisfied by a physically consistent C_{OX} is derived from the established theory, thereby completing the High-Low framework. The ‘complete’ framework’s theoretical validity is confirmed using simulated capacitance data for an n -SiC MOS structure, and the method’s frequency limitations are demonstrated. This analytical advancement ensures a physically consistent extraction of D_{IT} near the band edge, overcoming a fundamental limitation in MOS capacitor characterization.

1. Introduction

The characterization of interface state densities, D_{IT} , remains a fundamental requirement for the optimization of all metal-oxide-semiconductor (MOS) systems. The deleterious effects of interface states are particularly restrictive in wide-bandgap (WBG) semiconductors, such as silicon carbide (SiC) and gallium nitride (GaN), which are otherwise preferred materials for high-power transistors because of their high-breakdown capabilities and high-temperature resilience.¹⁻³ While SiC MOS field-effect transistors (MOSFETs) have achieved commercial success, their on-state performance fails to meet theoretical expectations due in great part to a high D_{IT} .⁴ As the applied gate bias approaches the threshold condition from the off-state, the subsequently charged interface states compensate as effective gate charge to shift the channel’s weak- and strong-inversion modes. In addition, these defects capture free carriers while also behaving as Coulomb scattering centers that reduce channel carrier mobilities, collectively lowering the device’s transconductance. These

* The following article has been submitted to the Journal of Applied Physics.

effects limit GaN MOSFETs as well, where similar to SiC, devices are characterized by slow ‘turn-on’ behavior with higher-than-expected on-resistance.^{5, 6}

Interface trap states that hinder an n -channel MOSFET are often studied using an n -type MOS capacitor. The n -type capacitor refers to the conductivity type in the bulk, whereas an n -channel MOSFET refers to the conductivity type of the inversion channel. For p -channel device development, p -type MOS capacitors are used. Figure 1 illustrates the characteristic structures and band diagrams for an n -type MOS capacitor biased at the onset of accumulation (or the flat-band condition) and a vertical n -channel power MOSFET biased at the onset of strong inversion. Interface states with energies closest to the band edge tend to have greater D_{IT} values, which is conveyed in the acceptor-like $D_{IT}(E)$ plot in Fig. 1. For shallow impurities, if the n -type doping concentration in the MOS capacitor equals the p -type doping concentration in the MOSFET channel region, then the energy range for accumulation in the MOS capacitor corresponds with the energy range for strong inversion in the MOSFET. Therefore, accumulation interface states for an n -type MOS capacitor can correspond to the D_{IT} most relevant to the performance degradation of an n -channel MOSFET. And yet, accumulation interface states are rarely reported in MOS capacitor D_{IT} analysis.

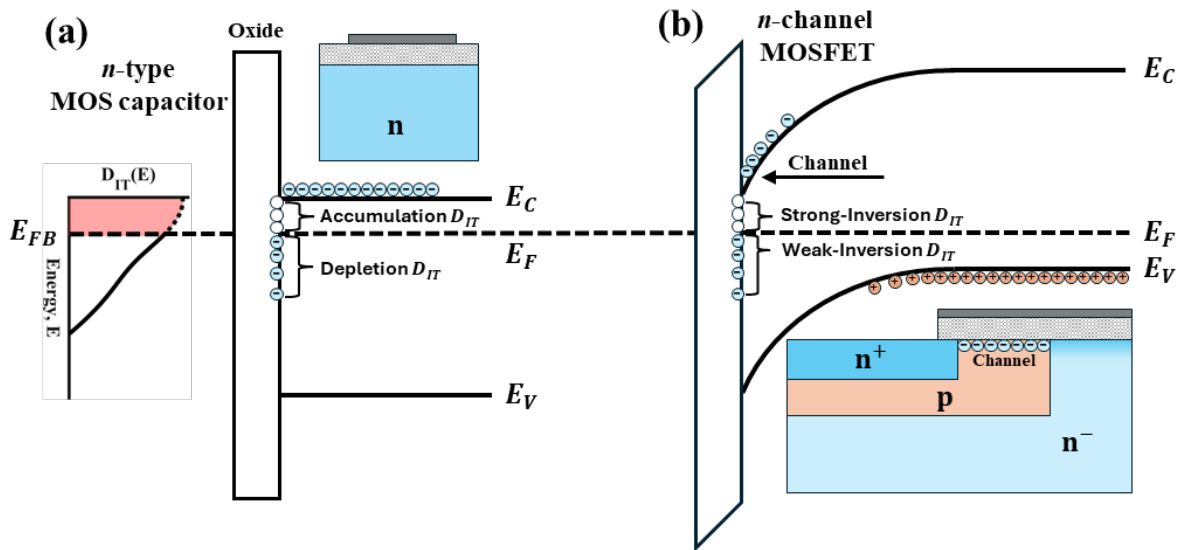


Figure 1: Band diagrams for (a) an n -type MOS capacitor biased at the flat-band condition and (b) a vertical n -channel MOSFET biased to the onset of strong-inversion. The $D_{IT}(E)$ plot on the left highlights the acceptor-like accumulation traps (red) of an n -type MOS capacitor, which correspond with traps most relevant to strong inversion in the corresponding n -channel MOSFET.

The High-Low C - V method is a standard technique for extracting $D_{IT}(E)$ from MOS capacitor structures, provided the high-frequency ac signal is sufficiently fast to ignore the capacitive contribution of interface states.⁷ This work highlights the known issue that an inaccurate oxide capacitance, C_{OX} , is a fundamental source of error that has not previously been resolved. Due to this error, the High-Low method, as it is conventionally used, cannot provide an accurate analysis for D_{IT} with energies in accumulation, regardless of how fast the measurement signal is. To resolve this dilemma, an electrostatic constraint is derived from well-established theory to complete the High-Low method. The validity of this constraint is then proven using simulated n -SiC data generated from an analytical model, and the completed framework accurately extracts D_{IT} for sufficiently fast high-frequency signals. The frequency limitations of the completed framework are then demonstrated, and analysis recommendations are made to accommodate fast interface states, such as completing the analysis at lower temperatures. While validated here using WBG parameters, the completed framework presented in this work provides a rigorous path for interface state analysis across all relevant MOS material systems.

2. The High-Low C - V Framework

The theory of MOS capacitors is recognized and supported by substantial literature,⁸⁻¹² and the following discussions largely draw from these sources. The present analysis addresses phenomena in accumulation and depletion, ignoring inversion, and focuses on n -type MOS structures.

a. The conventional, or ‘incomplete’, framework

The total MOS capacitance, C_{MOS} , is described using the small-signal (ac) circuit model, shown in Fig. 2. The oxide capacitance C_{OX} is in series with the semiconductor capacitance, C_S , which is itself the parallel sum of the space-charge capacitance, C_{SC} , and the interface trap capacitance, C_{IT} , i.e., $C_S(\psi_S) = C_{SC}(\psi_S) + C_{IT}(\psi_S)$. Therefore, C_{MOS} is given by

$$C_{MOS} = \left(\frac{1}{C_{OX}} + \frac{1}{C_S} \right)^{-1}. \quad (1)$$

The oxide layer acts as a simple, parallel-plate capacitor such that C_{OX} is independent of the electrostatics within the underlying semiconductor structure. Consequently, C_{OX} is constant with surface potential, ψ_S . Then, C_{SC} describes the capacitive response associated with the space-charge (or depletion) region that forms within the semiconductor substrate as a function of ψ_S . And lastly, $C_{IT}(\psi_S)$ is defined as

$$C_{IT}(\psi_S) = \left| \frac{dQ_{IT}}{d\psi_S} \right| = qD_{IT}(\psi_S), \quad (2)$$

where q is the fundamental charge constant. A series parasitic impedance, $Z(f_{ac})$, is observed for higher frequency measurements, which may be accounted for in experimental data^{8, 10}. A frequency-dependent conductance related to interface states is also part of the small-signal model, functioning in parallel with C_S . However, since the High-Low analysis does not consider this conductance, it is omitted in this work.

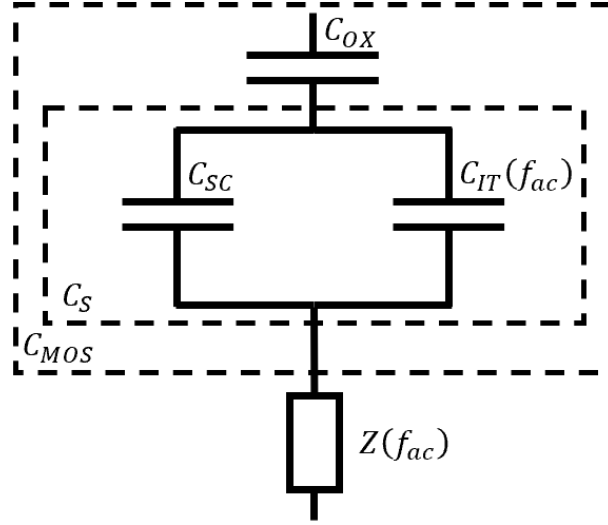


Figure 2: The small signal model describes C_{MOS} as being the series sum of the oxide capacitance C_{OX} and semiconductor capacitance C_S . A series parasitic impedance $Z(f_{ac})$ is observed at higher frequencies.

Contributions from C_{IT} to the small-signal model vary according to the frequency of the applied ac signal f_{ac} . For a low-frequency measurement, e.g., 1 Hz, interface states with energies over a broad range near the band edge are fast enough to capture and emit charge carriers during the ac oscillation and capacitively contribute to the C_{MOS} measurement. During a higher-frequency measurement, if the ac oscillation is too fast for the interface states to respond, their capacitive contributions are zero. In the High-Low method, a ‘true’ high-frequency measurement is one where the ac oscillation is fast enough so that all capacitive contributions from interface states are ignored. However, during any measurement, regardless of frequency, the dc-voltage-sweep ramp rate is slow enough such that dc-charged interface states contribute to the $V_G(\psi_S)$ relationship, leading to the C - V ‘stretch-out’ effect. In other words, despite a high-frequency measurement ignoring $C_{IT}(\psi_S)$, $D_{IT}(\psi_S)$ is still encoded in the subsequent $V_G(\psi_S)$ relationship.

The High-Low C - V method relies on measurements of both a low-frequency MOS capacitance, $C_{LF}(V_G)$, and a high-frequency MOS capacitance, $C_{HF}(V_G)$, to parameterize an experimental device.⁷ A fundamental assumption in utilizing this method is that C_{HF} represents a ‘true’ high-frequency measurement at least within the measured bounds of V_G . Assuming this condition is met, D_{IT} is defined as

$$D_{IT} = \frac{1}{q}(C_{S,LF} - C_{S,HF}), \quad (3)$$

where $C_{S,LF} = C_{SC} + C_{IT}$ and $C_{S,HF} = C_{SC}$ are the semiconductor capacitances for the low- and high-frequency measurements. Calculation of $C_{S,LF}$ and $C_{S,HF}$ from the experimental C_{MOS} data is done using (1), where a value for C_{OX} is usually obtained by estimation from measurement in accumulation.

Describing D_{IT} for specific trap energies relative to the bandgap first requires that a $\psi_S(V_G)$ relationship be defined. For analyses that utilize a low-frequency device measurement, this may be done using the Berglund equation,¹³

$$\psi_S(V_G) = \int_{V_G^+}^{V_G} \left(1 - \frac{C_{LF}(V_G)}{C_{OX}}\right) dV_G + \psi_S^+, \quad (4)$$

where V_G^+ is the maximum gate voltage measured in accumulation and ψ_S^+ is the surface potential that corresponds to V_G^+ . Then, ψ_S^+ can be experimentally determined by recognizing that the flat-band voltage, V_{FB} , corresponds with the flat-band capacitance, C_{FB} , of a ‘true’ high-frequency measurement, and $\psi_S(V_{FB})$ is equal to 0 V. The flat-band capacitance C_{FB} is defined as

$$C_{FB} = \left(\frac{1}{C_{OX}} + \frac{1}{C_{Debye}}\right)^{-1}, \quad (5)$$

where C_{Debye} is the Debye capacitance (see Appendix C). After identifying V_{FB} from the high-frequency curve, ψ_S^+ is chosen so that ψ_S is 0 V at $V_G = V_{FB}$. Finally, when ignoring quantum confinement effects, the calibrated ψ_S is linearly translated to the trap energy, E_T , described with respect to the relevant band edge (e.g., the conduction band edge, E_C , for an n -type semiconductor). The $E_C - E_T(\psi_S)$ relationship is defined as

$$E_C - E_T(\psi_S) = \left(\frac{E_g}{2} - \psi_f\right) - \psi_S, \quad (6)$$

where E_g is the semiconductor bandgap and ψ_f is the bulk Fermi level.

b. Completing the High-Low framework

It is well known that small variations in the user-approximated C_{OX} greatly affect the calculation of D_{IT} in accumulation using any capacitance-based method.^{10, 14} This is plainly evident in the relationship for C_S , rewritten from (1),

$$C_S = \frac{C_{OX}C_{MOS}}{C_{OX} - C_{MOS}}. \quad (7)$$

Regardless of the capacitive contribution from C_{IT} to C_S , when C_{MOS} is measured in accumulation so that it is nearer to C_{OX} , the determination of C_S is particularly sensitive to the choice for C_{OX} because $C_{OX} - C_{MOS}$ is very small compared to $\sqrt{C_{OX}C_{MOS}}$. Consequently, slight deviations in C_{OX} from the real value have a considerable impact on the error in calculating D_{IT} for trap energies very close to the band edge (i.e., in accumulation) and, to a lesser degree, for energies deeper in the bandgap. Furthermore, the mapping from V_G to $E_C - E_T$ is affected by the C_{OX} dependence in (4) and (5). Therefore, poor approximation of C_{OX} results in uncertainty when calculating both the D_{IT} near the band edge and the trap energy level when using C - V methods.

A simplistic method to approximate C_{OX} is by precisely measuring the dielectric thickness, t_{OX} , and then calculating $C_{OX} = \epsilon_{OX}\epsilon_0/t_{OX}$, where ϵ_0 is the permittivity of free space and ϵ_{OX} is the relative permittivity of the oxide. However, to be applicable for C - V analysis, ϵ_{OX} must be known with great precision, which necessitates reverse calculation starting with an accurate C_{OX} . Another common though misguided practice is to estimate C_{OX} as the maximum low-frequency capacitance measured far in accumulation, i.e., $C_{OX} = C_{LF}(V_G^+)$. The assumption that $C_{OX} = C_{LF}(V_G^+)$ is an invalid constraint, as it implies an infinitely large $C_S(V_G^+)$ and yields in infinite or negative D_{IT} close to the band edge. An approximation that $C_{OX} = f_{OX}C_{LF}(V_G^+)$, where f_{OX} is a correction factor, may improve the user-estimated C_{OX} , but there is nothing yet to indicate a correct value for f_{OX} . These errors become more pronounced (or f_{OX} gets larger) with increasing C_{OX} , as C_{MOS} tends to saturate in accumulation much sooner than anticipated as a consequence of Fermi-Dirac statistics and quantum confinement effects.¹⁵ Without a means to determine a physically consistent C_{OX} , the system of equations to conduct C - V analysis is underdetermined.

To complete the High-Low framework, an electrostatic constraint is derived in this work using fundamental relationships from established theory. During device operation, the externally applied V_G controls the internal system parameter ψ_S . The gate voltage V_G is the sum of voltage drops

across the oxide layer, V_{OX} , the semiconductor, V_S , and the built-in electric field across the MOS structure due to differences in the metal and semiconductor work functions, ϕ_{MS} . By applying Kirchoff's voltage law to enforce the conservation of energy across the structure, the gate voltage V_G is therefore related to ψ_S by the following:

$$V_G(\psi_S) = \phi_{MS} + V_{OX}(\psi_S) + V_S(\psi_S), \quad (8)$$

which, when considering acceptor-like interface traps, is expanded as

$$V_G(\psi_S) = \left[\phi_{MS} - \frac{Q_{OX}}{C_{OX}} + \frac{q}{C_{OX}} \int_{-\infty}^{\psi_S} D_{IT}(\psi_S) d\psi_S \right] + \psi_S - \frac{Q_S(\psi_S)}{C_{OX}}. \quad (9)$$

The bulk dielectric charge, Q_{OX} , describes the static charges in the oxide (e.g., fixed, mobile, trapped), which are screened as an effective sheet charge, and their charge remains constant with ψ_S . A brief discussion on the well-established derivation of (9) can be found in Appendix A. At the flat-band condition, or $\psi_S = 0$, the unbracketed terms evaluate to zero and the bracketed terms describes V_{FB} as

$$V_{FB} = \phi_{MS} - \frac{Q_{OX}}{C_{OX}} + \frac{q}{C_{OX}} \int_{-\infty}^0 D_{IT}(\psi_S) d\psi_S. \quad (10)$$

Notice that V_{FB} does not consider voltage drop due to interface states that exchange charge in accumulation, i.e., $D_{IT}(\psi_S > 0)$. Substituting (10) into (9) gives:

$$V_G(\psi_S) = V_{FB} + \frac{q}{C_{OX}} \int_0^{\psi_S} D_{IT}(\psi_S) d\psi_S + \psi_S - \frac{Q_S(\psi_S)}{C_{OX}}. \quad (11)$$

Equation (11) is then solved at the maximum surface potential ψ_S^+ to relate the physical and electronic features of an MOS capacitor at the maximum applied gate bias in accumulation V_G^+ ,

$$V_G^+ = V_{FB} + \frac{q}{C_{OX}} \int_0^{\psi_S^+} D_{IT}(\psi_S) d\psi_S + \psi_S^+ - \frac{Q_S^+}{C_{OX}}, \quad (12)$$

where Q_S^+ is $Q_S(\psi_S)$ solved at ψ_S^+ . The term ψ_S^+ is also the integration constant in (4). Finally, defining $\Delta V_{IT}^+ = \frac{q}{C_{OX}} \int_0^{\psi_S^+} D_{IT}(\psi_S) d\psi_S$ and rearranging (12) gives

$$\Delta V_{IT}^+ = (V_G^+ - V_{FB}) - \left(\psi_S^+ - \frac{Q_S^+}{C_{OX}} \right). \quad (13)$$

Equation (13) states that the voltage drop due to accumulation interface charge, ΔV_{IT}^+ , is equal to the flat-band-referenced voltage drop across the MOS structure, $V_G^+ - V_{FB}$, minus both the

semiconductor voltage drop, ψ_S^+ , and the oxide voltage drop from accumulated semiconductor charge, $-\frac{Q_S^+}{C_{OX}}$. Fundamentally, this relationship enforces the conservation of energy across the structure via Kirchoff's voltage law, establishing a strict electrostatic boundary. This constraint is derived from relationships that are inherent to MOS operation but are not considered within the traditional 'incomplete' High-Low method. Therefore, (13) provides the final constraint necessary to complete the High-Low framework without relying on physically arbitrary assumptions. A unique and physically consistent C_{OX} may be identified through a simple guess-and-check algorithm, illustrated in Fig. 3. The flowchart for this algorithm shows that the conventional (or 'incomplete') High-Low analysis is a subset of the 'complete' High-Low analysis. The determination of C_{OX} is demonstrated in the following section and visualized graphically.

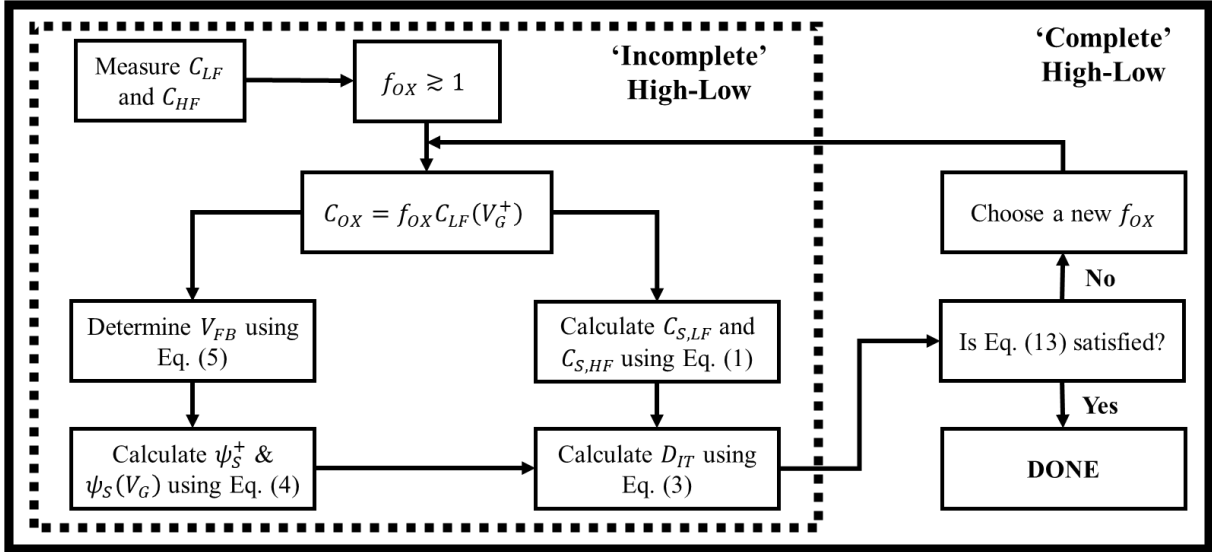


Figure 3: A flowchart showing the traditional, or 'incomplete', High-Low framework, as it is conventionally used, as a subset of the 'complete' High-Low framework. The symbol \approx is used to describe the correction factor f_{OX} as being approximately equal to though strictly greater than 1.

To calculate the right-hand side of (13), the $Q_S(\psi_S)$ relationship must be known. Neglecting quantum confinement effects, an analytical expression for $Q_S(\psi_S)$ can be described by solving Poisson's equation for the various operating modes of the MOS structure. When a device is operated such that the surface Fermi level is within $3kT$ of the band edge or is outside of the bandgap, the Maxwell-Boltzmann approximation is invalid and Fermi-Dirac statistics are used. The semiconductor charge $Q_S(\psi_S)$ is then defined for the degenerate case as

$$Q_S(\psi_S) = -\text{Sign}(\psi_S) \frac{kT}{q} \frac{\epsilon_S \epsilon_0}{L_D} \times \sqrt{\exp\left(\frac{q}{kT} \frac{E_g}{2}\right) [\mathcal{F}_{3/2}(\eta_S(\psi_S)) - \mathcal{F}_{3/2}(\eta_0)] - \exp\left(\frac{q\psi_f}{kT}\right) [\eta_S(\psi_S) - \eta_0]}, \quad (14)$$

where k is the Boltzmann constant, T is temperature, ϵ_S is the relative permittivity of the semiconductor, L_D is the intrinsic Debye length, and ψ_f is the bulk Fermi potential. The Fermi-Dirac integral of order j , $\mathcal{F}_j(\eta_S)$, is either solved using numerical methods or an analytical approximation.¹⁴ A discussion on calculating $\mathcal{F}_j(\eta_S)$ is found in Appendix B. The normalized surface Fermi level position referencing the conduction band edge, η_S , is given by

$$\eta_S(\psi_S) = -\frac{q}{kT} \left(\left(\frac{E_g}{2} - \psi_f \right) - \psi_S \right), \quad (15)$$

and $\eta_0 = \eta_S(0)$ is the normalized bulk Fermi level with respect to the conduction band edge.

If carrier confinement at the interface necessitates quantum confinement considerations, Q_S^+ must be calculated via a self-consistent solution of the Schrödinger and Poisson equations.¹⁵⁻¹⁷ In MOS structures, particularly under the strong electric fields required for moderate or strong accumulation, quantum confinement alters the spatial distribution of the carriers near the interface. Consequently, calculating Q_S^+ using the classical approximation in (14) overestimates the actual semiconductor charge. Still, the electrostatic constraint defined by (13) remains valid, and correctly accounting for quantum confinement effects in the ‘completed’ High-Low analysis yields a more accurate result. In the following analysis, quantum confinement considerations are omitted, and Q_S is defined using (14) strictly for the purpose of demonstrating the completed framework.

3. Demonstration of the ‘Complete’ High-Low Method

A self-consistent analysis that incorporates (13) is demonstrated using simulated MOS capacitor data so that the extracted parameters can be verified with the known input parameters. The analytical model emulates an n -type 4H-SiC MOS capacitor at room temperature where the uniform bulk donor impurity concentration, N_D , is $1 \times 10^{16} \text{ cm}^{-3}$, Q_{OX} and ϕ_{MS} are both zero, and C_{OX} is 100 nF/cm^2 to represent a 35-nm SiO₂ gate oxide. An analytical expression for the degenerate C_{SC} as well as the material properties used in this simulation are described in Appendices C and D, respectively. The input D_{IT} distribution and energy-dependent interface trap time constant distribution, τ_{IT} , are both shown in Fig. 4. The values are chosen to agree with the

distributions reported by Yoshioka et al., which were determined experimentally between $E_C - E_T = 0.16$ eV and 0.47 eV using the conductance technique.¹⁸ For D_{IT} outside of the reported energy range, a fitted distribution is assumed based on a two-Gaussian model yielding D_{IT} that increases as E_T moves closer to the band edge and decreases for E_T further in the bandgap. As a general approximation, τ_{IT} has an Arrhenius relationship with energy, which is reflected in the regions outside of the reported energy range.

The capacitive contribution from interface traps to the simulated device capacitance is calculated by

$$C_{IT}(\psi_S) = qD_{IT}(\psi_S) \left(1 - \exp\left(\frac{-1}{f_{ac}\tau_{IT}(\psi_S)}\right) \right), \quad (16)$$

where the exponential term acts as an ‘on/off’ function that imparts the characteristic effects of the input ac frequency f_{ac} . Similarly, the interface-state charge contribution to the $V_G(\psi_S)$ relationship is calculated by

$$Q_{IT}(\psi_S) = -q \int_{-\infty}^{\psi_S} D_{IT}(\psi_S) \left(1 - \exp\left(\frac{-\tau_{dc}}{\tau_{IT}(\psi_S)}\right) \right) d\psi_S, \quad (17)$$

where τ_{dc} is the characteristic residence time for the dc sweep at each gate voltage step. In a real measurement, τ_{dc} depends on the dc sweep rate and the V_G step size, and in this simulation, τ_{dc} is 1 s. According to the simulation results, the flat-band energy E_{FB} is about 0.2 eV below E_C and the flat-band voltage is 1.46 V.

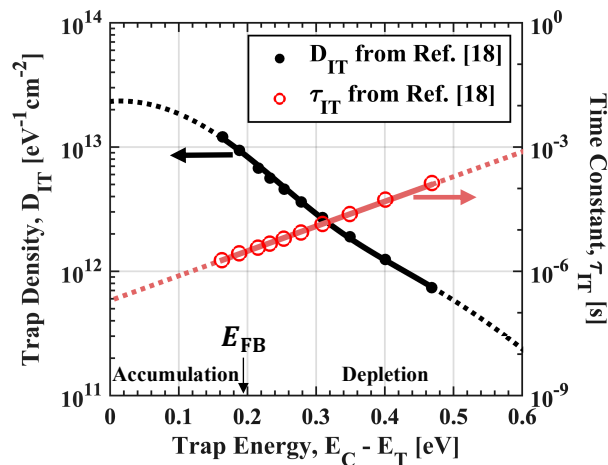


Figure 4: The analytical model’s input D_{IT} and τ_{IT} distributions are chosen to agree with values reported by Yoshioka et al.¹⁸ The dotted lines are extrapolations beyond the reported ranges. Energies to the left and right of E_{FB} are in accumulation and depletion, respectively.

A finely spaced range of ψ_S broadly spans the operating modes of strong accumulation, depletion, and deep depletion, and the corresponding $C_{SC}(\psi_S)$, $C_{MOS}(\psi_S)$ and $V_G(\psi_S)$ are calculated using (C6), (1) and (9), respectively. To emulate a real device measurement, C_{MOS} values are tabulated alongside V_G values from -10 V to 10 V with a step size of 100 mV. The simulated C - V curves for $f_{ac} = 1$ Hz, 100 kHz, 1 MHz, 10 MHz, and 100 MHz are shown in Fig. 5. A simulated 1 -THz signal is also included, which is fast enough to ignore the capacitive contribution from all interface states within the V_G limits of the generated data. Notice that the 1 -THz and 100 -MHz curves nearly overlap. The inset in Fig. 5 shows that the C_{MOS} curves near $V_G^+ = 10$ V do not exceed 99 nF/cm², and for moderately higher V_G^+ , C_{MOS} appears to stop increasing about 1% lower than the actual value of C_{OX} . The simulated C_{MOS} curves fail to converge with C_{OX} because C_{SC} saturates with V_G as a consequence of the Maxwell-Boltzmann approximation bounds being exceeded and Fermi-Dirac statistics prevailing.

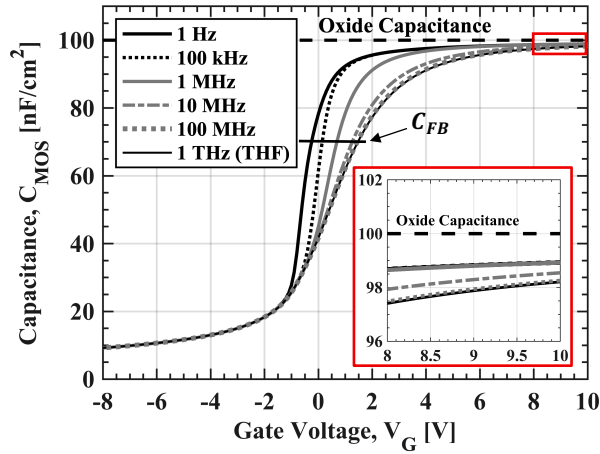


Figure 5: Frequency-dependent C - V curves are modeled using the D_{IT} and τ_{IT} distributions shown in Fig. 4. The ‘true’ high-frequency (THF) signal uses a 1 -THz input. The C_{FB} at 70.0 nF/cm² corresponds with a V_{FB} of 1.46 V for the 1 -THz curve. The inset shows C_{MOS} values near V_G^+ .

The ‘incomplete’ High-Low analysis is demonstrated using the ‘true’ high-frequency (1 THz) and the 1 -Hz low-frequency curves. The analysis is done for C_{OX} values ranging from 99.0 nF/cm² to 102.0 nF/cm², and the corresponding D_{IT} solutions are shown in Fig. 6(a). For the typical assumption that $C_{OX} \approx C_{LF}(V_G^+)$, i.e., 99.0 nF/cm², the ‘incomplete’ High-Low analysis reports a seemingly infinite D_{IT} for trap energies close to the band edge. As C_{OX} increases, D_{IT} near the band edge decreases, but only when the C_{OX} guess value matches the input value, i.e., 100.0 nF/cm², does the extracted D_{IT} match the input D_{IT} . It is noted that the errors of the reported

D_{IT} in Fig. 6 in depletion are small. The errors in this range are largely due to inaccuracies in calculating C_{FB} (and thus V_{FB}) using (5). For interfaces with larger D_{IT} in depletion, calculating V_{FB} can become more sensitive to C_{OX} and the subsequent errors in D_{IT} can become severe. Overall, these results demonstrate the most fundamental limitation of the ‘incomplete’ High-Low analysis, in that a ‘true’ high-frequency measurement is unable to recover D_{IT} in accumulation without a physically consistent C_{OX} .

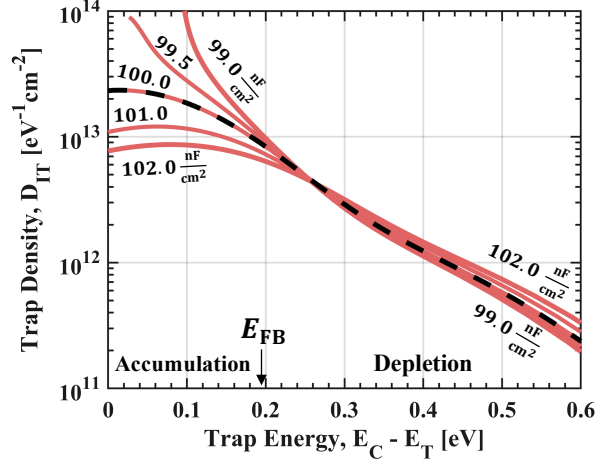


Figure 6: ‘Incomplete’ D_{IT} solutions (red) are solved using the simulated ‘true’ high-frequency and 1-Hz low-frequency curves for C_{OX} between 99.0 nF/cm^2 and 102.0 nF/cm^2 . The input D_{IT} (black dash) is only recovered when the input C_{OX} , i.e., 100.0 nF/cm^2 , is used.

The newly derived electrostatic constraint resolves this limitation, and its application is well visualized using the graphical technique illustrated in Fig. 7. First, ΔV_{IT}^+ may be calculated for any value of C_{OX} by numerically integrating the corresponding $\frac{q}{C_{OX}} D_{IT}(\psi_S)$ distribution between 0 and ψ_S^+ . A set of numerically calculated ΔV_{IT}^+ is then plotted (solid line) for a range of C_{OX} values. Next, at each C_{OX} value over the same range, the subsequent V_{FB} and ψ_S^+ values are used to analytically calculate ΔV_{IT}^+ value using (13), where V_G^+ is 10 V and Q_S^+ is solved for using (14). This second set of ΔV_{IT}^+ values is plotted (dashed line) alongside the first. The electrostatic constraint is satisfied at the intersection of these two curves, recovering the input C_{OX} and, consequently, the correct D_{IT} solution shown in Fig. 6. Thus, the ‘complete’ High-Low framework enables a physically consistent (or accurate) extraction of C_{OX} and measures D_{IT} into accumulation when using a ‘true’ high-frequency measurement.

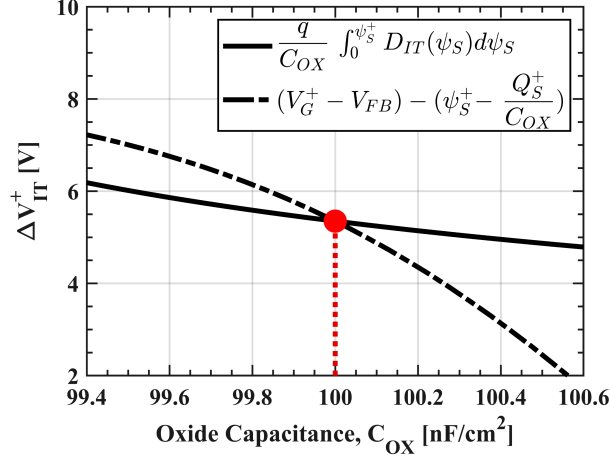


Figure 7: ΔV_{IT}^+ is solved both numerically from D_{IT} (solid) and analytically from (13) (dashed) over a range of C_{OX} . Their intersection at $C_{OX} = 100.0$ nF/cm² describes when the boundary constraint is satisfied, and the corresponding D_{IT} distribution in Fig. 6 matches the input D_{IT} distribution.

4. Accommodating Fast Traps using the ‘Complete’ High-Low Method

While the electrostatic constraint provides a completed picture of the High-Low framework, the analysis still requires that the high-frequency measurement be representative of a ‘true’ high-frequency response. To demonstrate this, analyses are conducted using the 100-kHz, 1-MHz, 10-MHz, and 100-MHz high-frequency data and the 1-Hz low-frequency data. The subsequent D_{IT} results are shown in Fig. 8. Application of the ‘complete’ High-Low technique using a 100-kHz or 1-MHz signal fails to adequately recover the input D_{IT} throughout the entire energy range. An insufficiently fast signal can still detect D_{IT} for traps that do not capacitively contribute to the high-frequency measurement. However, a suitably accurate V_{FB} will not be recovered, which impacts the calculations of ψ_S and, consequently, $E_C - E_T$. Therefore, the subsequent D_{IT} distribution is negatively shifted on the energy axis. On the other hand, the fast signals for the 10-MHz and 100-MHz measurements enable a satisfactory determination of V_{FB} and their D_{IT} results are nearly converged with the input D_{IT} near the conduction band edge. Also, the extracted C_{OX} values for these frequencies recover the input C_{OX} within 0.1%.

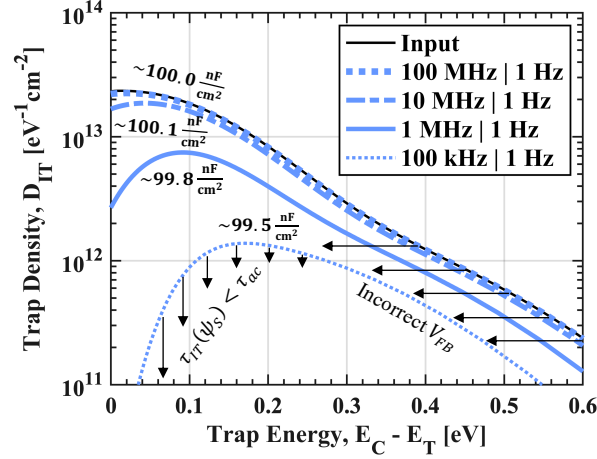


Figure 8: ‘Complete’ High-Low D_{IT} solutions using the simulated high-frequency measurements and the 1-Hz low-frequency measurement with their extracted C_{OX} values overlaid. For insufficiently fast high-frequency measurements, D_{IT} is negatively shifted on the energy axis due to an incorrect V_{FB} . Also, D_{IT} drops near the band edge due to the $\tau_{IT}(\psi_S)$ being smaller than the high-frequency signal time constant τ_{ac} (or $1/f_{ac}$).

The errors in D_{IT} for each of the high-frequency signals are contingent on the values of $\tau_{IT}(\psi_S)$. Here, the $\tau_{IT}(\psi_S)$ distribution is assumed from an Arrhenius fit of the values reported by Yoshioka et al.,¹⁸ resulting in signals as fast as 10 MHz being sufficient to extract D_{IT} within a reasonable margin of error. However, the time response for interface traps is inherent to the trap species present, and, according to extensive literature, the reported values for $\tau_{IT}(\psi_S)$ can vary substantially within and across different characterization techniques and WBG MOS systems.¹⁸⁻²¹ This is illustrated in Fig. 9 for 4H-SiC. In a separate report, Yoshioka et al. describe very fast trap states that are not detectable using a 10-MHz signal at room temperature, which they attribute to a nitrogen interstitial at the SiC surface as a result of nitric oxide annealing.²¹ Therefore, only if the high frequency is sufficiently fast relative to the frequency response of the traps, the ‘complete’ High-Low method can be used to accurately determine D_{IT} in accumulation. It should also be noted that this D_{IT} would not exclude capacitive contributions from slow border traps in the near-interfacial region, as they can also exchange charge during the low-frequency measurement.^{22, 23}

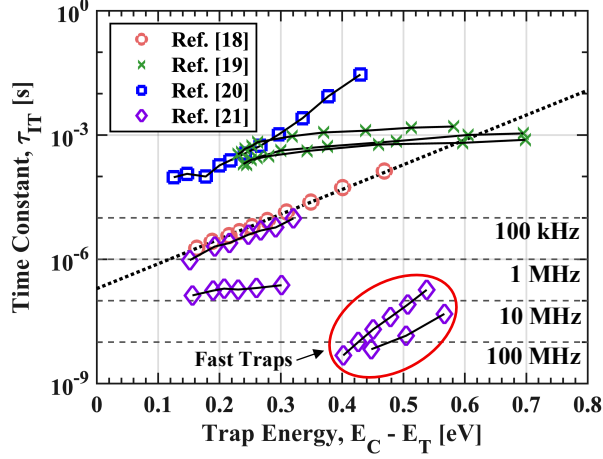


Figure 9: The range of reported values for $\tau_{IT}(\psi_S)$ at room temperature in $\text{SiO}_2/n\text{-SiC}$ MOS structures tend to increase exponentially with energy. The circled data refers to fast traps created by interfacial nitridation. The dashed line is the Arrhenius fit τ_{IT} distribution used in this work.

For SiC and GaN MOS systems containing fast interface traps, a 1-MHz measurement is insufficient at room temperature, and the ‘complete’ High-Low framework does not yield accurate results. In the absence of routine measurements exceeding 10 MHz, a quasistatic C - V method (e.g., the C - ψ_S method) shows promise.¹⁸ However, it is essential the correct form of C_{SC} that considers Fermi-Dirac statistics and quantum confinement effects is used as appropriate, and even still there are other unresolved issues in reporting D_{IT} in accumulation.²⁴ To extend the range of accessible trap energies, performing measurements at lower temperatures can increase trap response times.²¹ In yet another report by Yoshioka et al., it is shown that low-temperature conductance measurements allow the detection of fast interface traps with high-frequency signals as small as 1 MHz at 120 K.²⁵ In this regard, the successful application of the ‘complete’ High-Low method using routine frequencies at near-cryogenic temperatures appears likely and must be explored. Otherwise, developing higher-frequency (>100 MHz) measurement capabilities is of paramount importance for interface state analysis, even within the context of a completed theory.

5. Conclusion

In this work, an electrostatic constraint is derived using well-established theory to complete the High-Low analysis framework. The derivation recognizes that the dc voltage drop across an MOS structure biased in accumulation is explicitly linked to the voltage drop due to accumulation interface states. In turn, this constraint enables the determination of a physically consistent C_{OX} ,

which is imperative for extracting D_{IT} values in accumulation. The completed framework demonstrated in this work considers the Fermi-Dirac description for Q_S^+ to accommodate accumulation conditions, which are likely to violate the bounds of the Maxwell-Boltzmann approximation. However, for systems that exhibit quantum confinement effects, Q_S^+ must be calculated by self-consistently solving the Schrödinger and Poisson equations. The validity of the ‘complete’ High-Low framework is substantiated through simulated high- and low-frequency data generated from an analytical model. The proposed constraint rectifies a fundamental limitation of the High-Low technique, and the completed analysis results in an accurate D_{IT} profile in accumulation for sufficiently fast high-frequency measurements.

Appendix

A. A review of the $V_G(\psi_S)$ relationship

During device operation, an externally applied V_G controls the internal ψ_S , which dictates the operating modes of the MOS structure. The gate voltage V_G is the sum of voltage drops across the oxide layer, V_{OX} , the semiconductor substrate, V_S , and the built-in electric field across the MOS device due to differences in the metal and semiconductor work functions, ϕ_{MS} . Therefore, V_G may be described by the following relationship:

$$V_G(\psi_S) = \phi_{MS} + V_{OX}(\psi_S) + V_S(\psi_S). \quad (\text{A1})$$

The voltage drop across the semiconductor $V_S(\psi_S)$ is simply the difference in potential between the semiconductor surface and the semiconductor bulk, or

$$V_S(\psi_S) = \psi_S. \quad (\text{A2})$$

Then, the voltage drop across a dielectric layer is fundamentally described by Gauss’ law, which states that the electric field leaving a surface is proportional to the charge enclosed by that surface. Therefore, $V_{OX}(\psi_S)$ must consider the total charge in the semiconductor, Q_S , the static charged defects in the oxide, Q_{OX} , and the interface state charge, $Q_{IT}(\psi_S)$. The following relationship then describes V_{OX} :

$$V_{OX}(\psi_S) = -\frac{1}{C_{OX}}(Q_{OX} + Q_{IT}(\psi_S) + Q_S(\psi_S)). \quad (\text{A3})$$

The negative sign indicates that a positive charge on the gate corresponds to a negative charge in the underlying layers, and vice versa. The charge contribution of acceptor-like interface states Q_{IT} is a function of ψ_S by the relationship,

$$Q_{IT}(\psi_S) = -q \int_{-\infty}^{\psi_S} D_{IT}(\psi_S) d\psi_S, \quad (\text{A4})$$

where the negative sign refers to the respective polarity of the trapped charge. The lower integral limit in (A4) spans to $-\infty$ so that all interface charges with energies below ψ_S that can exchange charge are accounted for. Altogether, (A1) is expanded to be

$$V_G(\psi_S) = \left[\phi_{MS} - \frac{Q_{OX}}{C_{OX}} + \frac{q}{C_{OX}} \int_{-\infty}^{\psi_S} D_{IT}(\psi_S) d\psi_S \right] + \psi_S - \frac{Q_S(\psi_S)}{C_{OX}}. \quad (\text{A5})$$

B. Discussion on the Fermi-Dirac integral and its calculation

An analytical expression for the semiconductor charge Q_S at the semiconductor surface is derived by solving Poisson's equation while recognizing the appropriate boundary constraints.^{8,10,12} When Fermi-Dirac statistics are rigorously considered, the derivation involves the Fermi-Dirac integral. Generally, the Fermi-Dirac integral of the j^{th} order is defined as

$$\mathcal{F}_j(\eta_S) = \frac{1}{\Gamma(j+1)} \int_0^{\infty} \frac{\varepsilon^j}{1 + \exp(\varepsilon - \eta_S)} d\varepsilon, \quad (\text{B1})$$

where the gamma function, Γ , extends the factorial function to consider non-integer arguments. Then, $\varepsilon = (E - E_C)/kT$ is the normalized energy over which the improper integral is bounded, and $\eta_S = (E_S - E_C)/kT$ is the normalized surface energy at which the function is evaluated. For an n -type structure like the one studied in this work, both ε and η_S reference the conduction band edge, but for a p -type structure, these parameters reference the valence band edge, E_V . The derivative for $\mathcal{F}_j(\eta_S)$ with respect to η_S is given as

$$\frac{d\mathcal{F}_j(\eta_S)}{d\eta_S} = \mathcal{F}_{j-1}(\eta_S). \quad (\text{B2})$$

Extracting D_{IT} using the 'complete' High-Low method may require calculation of $\mathcal{F}_{3/2}(\eta_S(\psi_S))$. In general, numerical calculation of $\mathcal{F}_j(\eta_S)$ is completed very simply using common mathematical software (e.g., MATLAB). Alternatively, analytical approximations can provide estimations with a maximum error of $\sim \pm 0.5\%$.²⁶ An approximation for $\mathcal{F}_{3/2}(\eta_S)$ is the following:

$$\mathcal{F}_{3/2}(\eta_S) = \left[\exp(-\eta_S) + 15\sqrt{\pi/2} [(\eta_S + 2.64) + (|\eta_S - 2.64|^{2.25} + 14.9)^{4/9}]^{-5/2} \right]^{-1}. \quad (\text{B3})$$

Therefore, incorporating $\mathcal{F}_{3/2}(\eta_S(\psi_S))$ in the analysis is computationally straightforward and must not be avoided. Then, in the calculation of the degenerate space-charge capacitance C_{SC} discussed in Appendix C, $\mathcal{F}_{1/2}(\eta_S)$ must also be considered, which is similarly approximated as the following:

$$\mathcal{F}_{1/2}(\eta_S) = \left[\exp(-\eta_S) + 3\sqrt{\pi/2} [(\eta_S + 2.13) + (|\eta_S - 2.13|^{2.4} + 9.6)^{5/12}]^{-3/2} \right]^{-1}. \quad (\text{B4})$$

C. Analytical expressions for $C_{SC}(\psi_S)$

The space-charge capacitance $C_{SC}(\psi_S)$ is defined as

$$C_{SC}(\psi_S) = \left| \frac{dQ_S(\psi_S)}{d\psi_S} \right|. \quad (\text{C1})$$

For an n -type non-degenerate semiconductor, C_{SC} is described as

$$C_{SC}(\psi_S) = \frac{\epsilon_S \epsilon_0}{2L_D} \frac{\left| \exp\left(\frac{q\psi_f}{kT}\right) \left(\exp\left(\frac{q\psi_S}{kT}\right) - 1 \right) \right|}{\sqrt{\exp\left(\frac{q\psi_f}{kT}\right) \left(\exp\left(\frac{q\psi_S}{kT}\right) - \frac{q\psi_S}{kT} - 1 \right)}}, \quad (\text{C2})$$

where the intrinsic Debye Length L_D is defined as

$$L_D = \sqrt{\frac{\epsilon_S \epsilon_0 kT}{2q^2 n_i}}, \quad (\text{C3})$$

which must not be confused with the extrinsic Debye length $L_{D,\text{Ext.}}$ used in the calculation of $C_{\text{Debye}} = \epsilon_S \epsilon_0 / L_{D,\text{Ext.}}$, where $L_{D,\text{Ext.}}$ is defined as

$$L_{D,\text{Ext.}} = \sqrt{\frac{\epsilon_S \epsilon_0 kT}{q^2 N_D}}. \quad (\text{C4})$$

The bulk Fermi potential ψ_f for an n -type semiconductor is defined as

$$\psi_f = \frac{kT}{q} \ln\left(\frac{N_D}{n_i}\right). \quad (\text{C5})$$

For an n -type degenerate semiconductor that does not consider quantum confinement effects, C_{SC} is found by plugging (14) into (C1) while making use of (B2), which gives

$$C_{sc}(\psi_s) = \frac{\epsilon_s \epsilon_0}{2L_D} \frac{\left| \exp\left(\frac{qE_g}{2kT}\right) \mathcal{F}_{1/2}(\eta_s(\psi_s)) - \exp\left(\frac{q\psi_f}{kT}\right) \right|}{\sqrt{\exp\left(\frac{qE_g}{2kT}\right) [\mathcal{F}_{3/2}(\eta_s(\psi_s)) - \mathcal{F}_{3/2}(\eta_0)] - \exp\left(\frac{q\psi_f}{kT}\right) [\eta_s(\psi_s) - \eta_0]}}. \quad (C6)$$

D. Simulation Parameters

Table 1: Simulation parameters used in the analytical model based on an n-type 4H-SiC MOS capacitor at room temperature.

Parameter	Symbol	Value
Oxide Capacitance	C_{OX}	$100 \frac{\text{nF}}{\text{cm}^2}$
Semiconductor Bandgap	E_g	3.23 eV
Intrinsic Carrier Concentration	n_i	$4.82 \times 10^{-9} \frac{1}{\text{cm}^3}$
Effective Density of States in the Conduction Band	N_C	$1.63 \times 10^{19} \frac{1}{\text{cm}^3}$
Effective Density of States in the Valence Band	N_V	$2.41 \times 10^{19} \frac{1}{\text{cm}^3}$
Bulk Equilibrium Electron Density	N_D	$1 \times 10^{16} \frac{1}{\text{cm}^3}$
Static Oxide Charge	Q_{OX}	0
Device Temperature	T	293 K
Semiconductor Dielectric Constant	ϵ_s	9.7
Characteristic DC Sweep Residence Time	τ_{dc}	1 s
Metal-Semiconductor Work Function	ϕ_{MS}	0

Nomenclature

- C_{FB} – Flat-band capacitance
 C_{LF} – Low-frequency device capacitance
 C_{HF} – High-frequency device capacitance
 C_{IT} – Interface trap capacitance
 C_{MOS} – MOS capacitance measured from a device
 C_{OX} – Oxide capacitance
 C_S – Semiconductor capacitance
 C_{SC} – Space-charge (or depletion) capacitance
 D_{IT} – Density of interface traps
 E_C – Conduction band-edge energy
 E_g – Semiconductor bandgap
 E_f – Semiconductor Fermi energy
 E_{FB} – Flat-band energy
 E_i – Intrinsic semiconductor Fermi energy
 E_T – Interface trap energy
 E_V – Valence band-edge energy
 f_{ac} – AC signal frequency
 f_{OX} – C_{OX} correction factor
 \mathcal{F}_j – Fermi-Dirac integral of order j
 k – Boltzmann constant
 L_D – Intrinsic Debye length
 n_i – Intrinsic carrier concentration
 N_C – Effective density of states in the conduction band
 N_V – Effective density of states in the valence band
 N_A – Bulk equilibrium hole density
 N_D – Bulk equilibrium electron density
 Q_{IT} – Interface trapped charge
 Q_{OX} – Static oxide charge
 Q_S – Semiconductor charge
 Q_S^+ – Semiconductor charge at ψ_S^+

q – Fundamental charge constant
 t_{OX} – Oxide layer thickness
 T – Device temperature
 V_{FB} – Flat-band voltage
 V_G – Gate voltage
 V_G^+ – Maximum gate voltage measured in accumulation
 V_{OX} – Voltage drop across the oxide
 V_S – Voltage drop across the semiconductor
 ΔV_{IT}^+ – Voltage drop due to measured accumulation interface states
 ϵ_S – Semiconductor dielectric constant
 ϵ_{OX} – Oxide dielectric constant
 ϵ_0 – Permittivity of free space
 η_S – Normalized surface Fermi level position
 η_0 – Normalized bulk Fermi level position
 τ_{dc} – Characteristic residence time of the dc sweep
 τ_{IT} – Interface trap time constant
 ϕ_{MS} – Gate-to-semiconductor work function
 ψ_f – Fermi potential of the bulk substrate
 ψ_S – Fermi potential at the substrate surface
 ψ_S^+ – The Berglund constant, or the Fermi potential at the surface corresponding with V_G^+

Acknowledgements

Sandia National Laboratories is a multi-mission laboratory managed and operated by the National Technology and Engineering Solutions of Sandia, LLC, a wholly owned subsidiary of Honeywell International Inc., for the U.S. Department of Energy’s National Nuclear Security Administration under Contract DE-NA0003525. This article describes objective technical results and analysis. Any subjective views or opinions that might be expressed in the article do not necessarily represent the views of the U.S. Department of Energy or the U.S. Government.

Sarit Dhar gratefully acknowledges the support provided by the Auburn University Professional Improvement Leave program.

The authors sincerely thank Dr. James Loveless at Sandia National Laboratories for invaluable discussions related to the analytical model.

Author Declarations

Conflicts of Interest

The authors have no conflicts to disclose.

Author Contributions

Brian D. Rummel: Conceptualization (lead); Formal Analysis (lead); Investigation (lead); Methodology (lead); Software (lead), Visualization (lead); Writing – Original Draft Preparation (lead); Writing – Review & Editing (lead). **Sarit Dhar:** Validation (equal); Writing/Review & Editing (supporting). **Robert J. Kaplar:** Validation (equal); Writing/Review & Editing (supporting).

Data Availability

The data that support the findings of this study are available from the corresponding author upon reasonable request.

References

1. J. A. Cooper and D. T. Morissette, *IEEE Electron Device Letters* **41** (6), 892-895 (2020).
2. J. Millan, P. Godignon, X. Perpina, A. Perez-Tomas and J. Rebollo, *IEEE Transactions on Power Electronics* **29** (5), 2155-2163 (2014).
3. M. Buffolo, D. Favero, A. Marcuzzi, C. De Santi, G. Meneghesso, E. Zanoni and M. Meneghini, *IEEE Transactions on Electron Devices* **71** (3), 1344-1355 (2024).
4. T. Kimoto and J. A. Cooper, *Fundamentals of Silicon Carbide Technology*. (2014).
5. J. Li, Q. Guo, C. Wang, Z. Hu, Q. Wu, L. Liu, J. Wan, H. Xu, H. Wang, N. Ren and K. Sheng, *IEEE Transactions on Electron Devices* **71** (10), 6221-6227 (2024).
6. R. Zhu, H. Jiang, C. W. Tang and K. M. Lau, *IEEE Electron Device Letters* **43** (3), 346-349 (2022).
7. R. Castagné and A. Vapaille, *Surface Science* **28** (1), 157-193 (1971).
8. D. K. Schroder, *Semiconductor Material and Device Characterization*, 3rd Edition ed. (IEEE Press, 2015).
9. S. M. Sze and M.-K. Lee, *Semiconductor Devices - Physics and Technology*, 3rd Edition ed. (2012).

10. E. H. Nicollian and J. R. Brews, *MOS (Metal Oxide Semiconductor) Physics and Technology*. (Wiley Interscience, 1982).
11. E. H. Nicollian and A. Goetzberger, *Applied Physics Letters* **7** (8), 216-219 (1965).
12. R. Pierret, *Semiconductor Device Fundamentals*, 2nd ed. (Addison Wesley, 1996).
13. C. N. Berglund, *IEEE Transactions on Electron Devices* **ED-13** (10), 701-705 (1966).
14. M. J. McNutt and C. T. Sah, *Journal of Applied Physics* **46** (9), 3909-3913 (1975).
15. O. Simonetti, T. Maurel and M. Jourdain, *Journal of Applied Physics* **92** (8), 4449-4458 (2002).
16. Y. Li, J.-W. Lee, T.-W. Tang, T.-S. Chao, T.-F. Lei and S. M. Sze, *Computer Physics Communications* **147** (1-2), 214-217 (2002).
17. T. Dutta, C. Medina-Bailon, N. Xeni, V. P. Georgiev and A. Asenov, in *2021 IEEE 16th Nanotechnology Materials and Devices Conference (NMDC)* (2021), pp. 1-4.
18. H. Yoshioka, T. Nakamura and T. Kimoto, *Journal of Applied Physics* **111** (1) (2012).
19. E. Bano, T. Ouisse, L. Di Cioccio and S. Karmann, *Applied Physics Letters* **65** (21), 2723-2724 (1994).
20. P. Zhao, Rusli, Y. Liu, C. C. Tin, W. G. Zhu and J. Ahn, *Microelectronic Engineering* **83** (1), 61-64 (2006).
21. H. Yoshioka, T. Nakamura and T. Kimoto, *Journal of Applied Physics* **112** (2) (2012).
22. D. M. Fleetwood, *Microelectronics Reliability* **80**, 266-277 (2018).
23. D. M. Fleetwood, P. S. Winokur, R. A. Reber, T. L. Meisenheimer, J. R. Schwank, M. R. Shaneyfelt and L. C. Riewe, *Journal of Applied Physics* **73** (10), 5058-5074 (1993).
24. B. D. Rummel, J. A. Cooper, D. T. Morissette, L. Yates, C. E. Glaser, A. T. Binder, K. Ramadoss and R. J. Kaplar, *J. Appl. Phys.* **134** (12), 125302 (2023).
25. H. Yoshioka, T. Nakamura and T. Kimoto, *Journal of Applied Physics* **115** (1) (2014).
26. J. S. Blakemore, *Solid-State Electronics* **25** (11), 1067-1076 (1982).